Preparation and study on the properties of bulk amorphous alloy $Fe_{78}Si_9B_{13}$ by ultrasonic welding

ZHENGQIANG ZHU [a], YANJUN WANG[a], YIFU ZHANG[b]
[a]*School of Mechanics Engineering, Nanchang University, Nanchang, Jiangxi 330031, China*
[b] *School of Mechanics & Materials Engineering, Jiujiang University, Jiujiang, Jiangxi 332005, China*

The low temperature, low pressure and low energy consumption associated with ultrasonic welding make it suitable for solid state joining of multi-layer $Fe_{78}Si_9B_{13}$ amorphous alloy foil. In this study, surface and volume effects created by ultrasonic welding process have been successfully utilized to prepare bulk amorphous alloys. The thermodynamic properties of materials and welding transient temperature distributions were analyzed using the welding joint structure and morphology, to determine the optimum parameters of ultrasonic welding: $n=5$；$A=35\mu m$; $f=20$ kHz; $F=1.37\times10^3N$; $t=220ms$. Based on the material model and heat source model of amorphous alloy foil, an axisymmetric thermal - structural finite element model of multi-layer $Fe_{78}Si_9B_{13}$ amorphous foil was developed for ultrasonic welding. The FEM model was prepared using a finite element analysis software ANSYS to simulate the ultrasonic welding process of multi-layer $Fe_{78}Si_9B_{13}$ amorphous foil. The current study demonstrates, through experimental data, the effect of different welding times on the temperature field distribution of multi-layer foils during ultrasonic welding of multilayer alloy foils.

1. Introduction

Amorphous alloys, also known as metallic glasses, are defined by a short-range ordered and a long-range disordered metastable structure. This three-dimensional metastable array of disordered atoms remains relatively stable within a certain temperature range. Many scholars have carried out detailed studies of these structures and properties [1-2]. These alloys are known to have excellent physical and mechanical properties such as high hardness, high strength, good wear and corrosion resistance, good soft magnetic properties and super-plasticity, among others. These materials have a wide range of applications in various fields such as mechanical, electronic, aerospace and defense industry. There is considerable research interest in exploring energy efficient techniques for joining/ creating metallurgical bonds in these amorphous alloys.

1960s, American professor Duwez [3] showed that amorphous silicon alloys could be produced by cooling a liquid alloy at rates higher than its critical cooling rate. When the cooling rate is higher than $10^2K/s$, it is possible to avoid heterogeneous nucleation. Under such conditions, crystallization in the melt is hindered during solidification leading to super-cooling of the melt leading to an amorphous structure. This imparts the melt a strong amorphous forming ability. This process is usually high efficiency and low cost and up to 0.1m thick blocks of amorphous material can be obtained. Over the years,

tremendous progress has been made in this field. Pd-Ni-P alloys were the first class of bulk amorphous alloys produced. Turnbull et al. [4] purified amorphous alloy melts by boron oxide coating method. Later, several other multi-component amorphous alloys were developed including zirconium-based[5], magnesium-based[6], aluminum-based[7], iron-based[8] and copper-based[9]. In 1993, Peker etc. [10] found an $Zr_{41.2}Ti_{13.8}Cu_{12.5}Ni_{10}Be_{22.5}$ amorphous alloy system, known to have the best glass forming ability, so achieve the glassy state oxide forming ability, as long as the cooling rate is not less than 1 k/s, can avoid crystallization.

Studies have shown that amorphous alloys can be produced using laser welding, explosion welding, friction welding, ultrasonic welding and other joining methods. Yoshihito Kawamura et al. [11] pioneered the process of making amorphous alloy system $Zr_{55}Al_{10}Ni_5Cu_{30}$ using pulse welding technique. The thus created weld joint and heat affected zone have no holes, cracks or slag phenomenon, and the joint tensile strength is the same as that of the starting amorphous materials. B. Li et al. [12] successfully produced amorphous block of $Zr_{45}Cu_{48}Al_7$ using a laser welding method. Yoshihiko Yokoyama et al. [13] used flakes of amorphous $Zr_{50}Cu_{30}Ni_{10}Al_{10}$ to create bulk amorphous materials using electron beam welding. Y. Kawamura et al. [14] joined $Zr_{41}Be_{23}Ti_{14}Cu_{12}Ni_{10}/2017Al$ and $Zr_{41}Be_{23}Ti_{14}Cu_{12}Ni_{10}/5083Al$, by friction welding method

effectively. After welding, crystallization of the melt does not take place and the material retains its amorphous structure from the melt. D. Wang et al. [15] used friction stir welding to join amorphous $Zr_{55}C\mu_{30}Al_{10}Ni_5$ to a plate of Al-Zn-Mg-Cu. Hyung Seop Shin et al. [16] used friction welding method to join bars of Zr-based amorphous material to obtain larger sized bulk of the same. Takuo Shoji et al. [17] performed a variety of friction welding tests on zirconium-based amorphous rods and studied the post-weld joints. They did not observe any combination of surface cracks, inclusions or crystallization phenomenon in the thus created joints. The joint surface rupture tests indicated that the joint has rupture characteristics similar to that of the bulk amorphous material and also have similar tensile strength.

The glass transition temperature is a key factor in achieving an effective heterogeneous BMG joint. When the temperature difference is not greater than 50K, amorphous materials can be joined successfully. Yoshihito Kawamura [18] and C.H.Wong et al. [19] effectively use friction welding to join homogeneous amorphous alloy systems in order to get a larger sized bulk amorphous rod. Again, the joint weld zones and heat affected zones were not crystallized, and cracks, shrinkage and impurities phenomenon were not found. The tensile strength of the welded bulk material was similar to that of the original bulk.

When amorphous alloy are subjected to the conditions of high temperature or slow cooling, a process of crystallization takes place. In this process the atoms get re-organized and the original metastable amorphous structure is lost giving way to a stable crystalline structure. Upon crystallization, the material loses its excellent mechanical and physical properties associated with the amorphous structure. Ultrasonic welding under static pressure is a process where the mechanical energy of an ultrasonic vibration is converted into heat due to friction and deformation welding interface. This technique is known to efficiently form joints in a solid state without causing any melting [20]. Amorphous alloys can be effectively joined with this technique and can still retain their disordered structure. This is a low cost, no pollution and high efficiency process. Kreye [20] pioneered the technique of joining using ultrasonic technology and successfully connected chip and copper. Masakatsu Maeda et al. [21] effectively joined a zirconium based amorphous alloy $Zr_{55}Cu_{30}Ni_5Al_{10}$, but the joint area was small.

Multilayer joining of $Fe_{78}Si_{13}B_9$ sheets using ultrasonic welding, discussed in this paper, is a complex yet short process. It is difficult to measure the temperatures of the melt pool created during the welding process. When using ultrasonic welding method for joining amorphous alloys, the temperature distribution at the joint interface is important in determining effective joining of the alloys as well as the retention of the amorphous structure. So for the ultrasound preparation analog of amorphous alloy is also very necessary.

2. Experimental procedure

2.1. Preparation of amorphous $Fe_{78}Si_9B_{13}$ alloys by ultrasonic welding

For the present study, $Fe_{78}Si_9B_{13}$ amorphous alloy foil sheets with dimensions of $120 \times 25 \times 0.025mm$ were used. The schematic of the ultrasonic welding process is shown in Fig. 1. To facilitate welding of multi layers of $Fe_{78}Si_9B_{13}$ amorphous alloy foil, the following experimental procedure was followed:

(1) Wipe out the surface oxide film on the amorphous alloy foils for effective weld;

(2)Ultrasonic welding parameters: n(superimposed layers of foil)=2–6, A(ultrasonic amplitude)=35μm, f(ultrasonic vibration frequency)=20kHz, F(welding static pressure)= 0.92×10^3N–1.72×10^3N, t(Welding time)= 0–220ms.
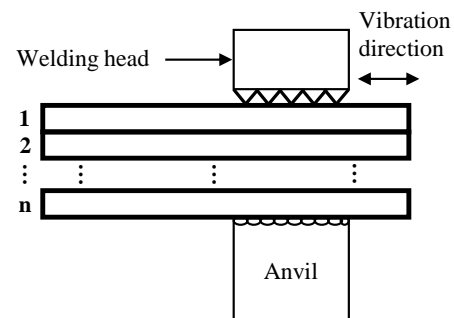

Fig. 1. A schematic showing an ultrasonic welding process.

An optical microscope and a scanning electron microscope were used to observe the morphology/microstructure of the $Fe_{78}Si_{13}B_9$ amorphous alloy foil sheet after being ultrasonically welded. It is known that the diffraction spectra of crystalline materials show sharp peaks. However, an amorphous material is signified by a single large diffused peak. This knowledge acts as an important differentiation to evaluate if any crystallization has taken place after welding of the amorphous foils. For current experiments, a Bruker AXS (Germany) D8-FOCMS type micro -X-ray diffractometer was used to analyze the post weld structure of multilayer $Fe_{78}Si_{13}B_9$ amorphous foil. Changes in the thermal properties after welding joints were studied in a high temperature differential scanning calorimeter DSC404F3. DSC curves of the original amorphous material as well as those from the welded joints of multilayer $Fe_{78}Si_{13}B_9$ sheets were taken. Micro Vickers Hardness of welded

multilayer Fe$_{78}$Si$_{13}$B$_9$ foils was measured using an HVS-1000 type micro hardness tester. Raytek 3I2M series of portable infrared thermometer was used to detect the temperature of multilayer Fe$_{78}$Si$_{13}$B$_9$ foils during ultrasonic welding. The flowchart in Fig. 2 shows the testing process that was followed for the study presented here.
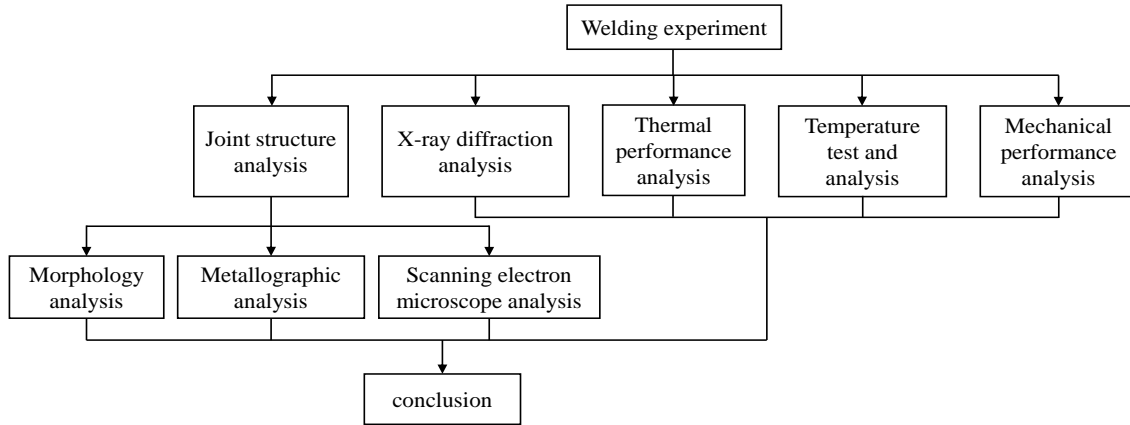

Fig. 2. Flow chart showing the testing process.

2.2. The FEM simulation of the welding process

While the heat generated by the friction between amorphous sheets during ultrasonic welding process helps form a joint, it adversely affects the structure of the amorphous foils. The interaction between morphology of materials and thermal changes formed a staggered heat - structure coupling process. Following assumptions for the simplification of the model were made:

(1) The room temperature of welding is 20 °C;

(2) There is no gap or relative sliding between the welding head, multi-layer sheet and Anvil;

(3) The cross-section of ultrasonic horn is levelled and has a uniform texture;

(4) The plastic deformation zone of multilayer sheets and welding head cross-sectional area are equal during welding;

(5) There is symmetry of temperature field, and simulation for symmetrical geometric structure.

Table 1. Thermal performance parameters of horn and anvil.

Temperature (°C)	Density (kg/m^{-3})	Thermal expansion coefficients (10^{-5}/T)	Thermal Conductivity (W/m· k)	Specific heat capacity (J/kg· k)
20	7800	1.48	34	460
300	-	1.51	36.2	513
500	-	1.58	38.1	532
800	-	1.65	39.5	560
1200	-	1.72	40.7	584

Table 2. Convective heat transfer coefficient of horn and anvil.

Temperature (°C)	300	400	500	600	700	800	900
Convection coefficient (W/m^2·°C)	8.58	8.92	9.12	9.03	9.04	8.99	8.87

The thermal performance parameters of welding head and anvil are shown in Table 1. The convective heat transfer coefficients of welding head and anvil are shown in Table 2. It can be seen from the two tables that, when the surface temperature is between 300°C–900°C; natural convection heat transfer coefficient is about 9W/m^2.°C. This value is used as a constant in the simulation presented here.

There is little effect of temperature on the density of the amorphous alloy Fe$_{78}$Si$_9$B$_{13}$ at these temperatures. Hence a constant value of density at 7.18g/cm^3 was used in the simulation analysis. Curves in Fig. 3(a), (b) and (c)

show the variation of thermal expansion coefficient, thermal conductivity and specific heat, respectively, of the $Fe_{78}Si_9B_{13}$ amorphous alloy with temperature. It can be seen that the specific heat capacity of amorphous $Fe_{78}Si_9B_{13}$ changes dramatically with increasing temperature. The specific heat capacity increases rapidly in the super-cooled liquid region, and then quickly decreases in the molten state. 420°C and 495°C, respectively, are used as the glass transition and the initial temperature of crystallization of the amorphous material. The natural convection coefficient of bulk amorphous alloy in air is taken to be $13W/m^2 \cdot K$ for the current simulation.
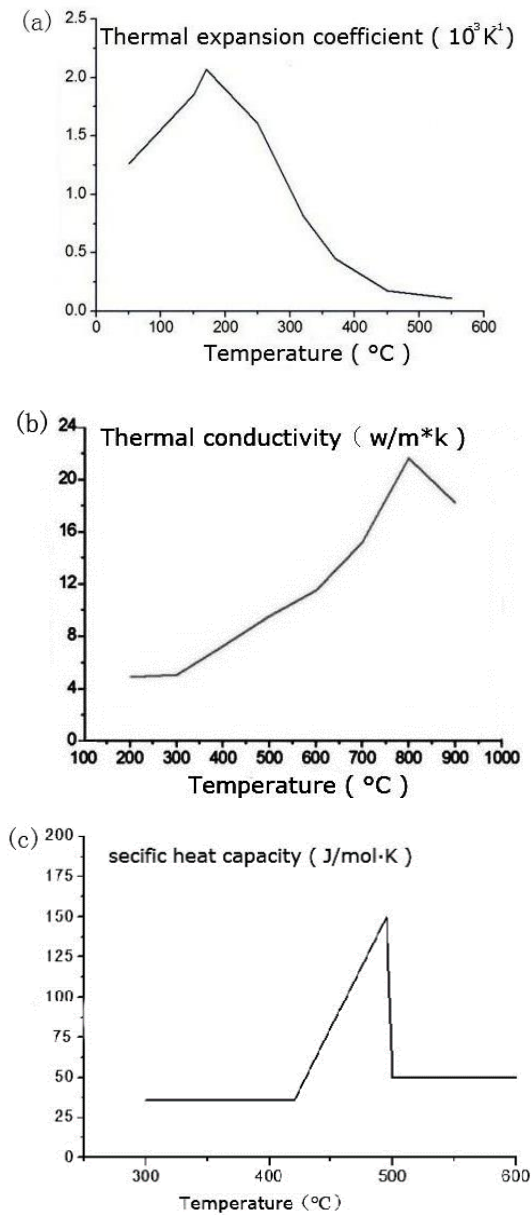
Fig. 3.The thermal physical properties parameters of $Fe_{78}Si_9B_{13}$ amorphous alloy .

Ultrasonic welding process produces heat due to the plastic deformation caused by ultrasonic vibration [23].

(1) Plastic deformation heat flux

During ultrasonic welding of multilayer $Fe_{78}Si_9B_{13}$ foil, the material deforms under uniform vertical static pressure and horizontal alternating shear force, such that the plastic deformation and accompanied heat load is evenly distributed. The heat flux density of multi-layer foil during plastic deformation is given by:

$$Q_W = \frac{P_t}{A_w} = \frac{F_W \times V_{avg}}{A_w} \tag{1}$$

Where, Q_W–heat flux due to deformation (W/mm^2); P_t–power (W) A_W–welding head area (mm^2); F_W–plastic deformation welding force(N); V_{avg}–average sonotrode velocity (m/s)

$$F_W = \sqrt{(\frac{Y_T}{2})^2 - (\frac{F_N / A_{DZ}}{2})^2} \times A_{DZ} \tag{2}$$

$$V_{avg} = 4 \times \varepsilon_0 \times f_w \tag{3}$$

Where, F_N–welding static pressure(N); Y_T–yield strength(N/mm^2); A_{DZ}–plastic deformation area (mm^2); ε_0–ultrasonic amplitude (μm); f_w–ultrasonic vibration frequency (Hz).

In the initial stage of ultrasonic welding, deformation is limited to in-between the bumps on the surface. However, as the welding progresses, this deformation extends to the whole area of the horn. The plastically deformed area is determined by the formula:

$$A_{DZ}(t) = 1.6 \times 10^5 \times (1 - e^{-kt}) \tag{4}$$

Where, A_{DZ}–plastic deformation area (mm^2); k–thermal conductivity (W/(m K));t–time (s); k–Constant values

When the multilayer foils are welded, plastic deformation gradually decreases from the top to the bottom layer, so the plastic deformation heat flux density of the n-th layer is given by:

$$Q_w^n = \frac{Q_W}{2^{n-1}} \tag{5}$$

Where, Q_W–heat flux due to deformation (W/mm^2); n–Foil layers

By equation (1), (2), (3), (4) and (5), when the multilayer foils are ultrasonically welded, plastic deformation heat flux of the n-th layer is given by:

$$Q_w^n(t) = \frac{6.4 \times 10^5 \times \sqrt{(Y_T/2)^2 - ((F_N/1.6 \times 10^5 \times (1-e^{-kt}))/2)^2} \times (1-e^{-kt}) \times \varepsilon_0 \times f_w}{2^{n-1} \times A_w} \qquad (6)$$

(2) Frictional heat flux

In the ultrasonic welding process of the multilayer Fe$_{78}$Si$_9$B$_{13}$ foil, assuming that the heat input at the joint is not caused by plastic deformation, but caused by friction, we get:

$$A_{FR}^n = \frac{A_{DZ}}{2^n} \qquad (7)$$

Friction heat flux during ultrasonic welding:

$$Q_{FR} = \frac{P_{FR}}{A_{FR}} = \frac{F_{FR} \times V_{avg}}{A_{FR}} = \frac{\mu \times F_N \times V_{avg}}{A_{FR}} \qquad (8)$$

By equation (3), (4), (7), (8), when the multilayer foils ultrasonic welding, friction heat flux of the n-th layer:

$$Q_{FR}^n(t) = \frac{2^n \times \mu \times F_N \times \varepsilon_0 \times f_w}{4 \times 10^4 \times (1-e^{-kt})} \qquad (9)$$
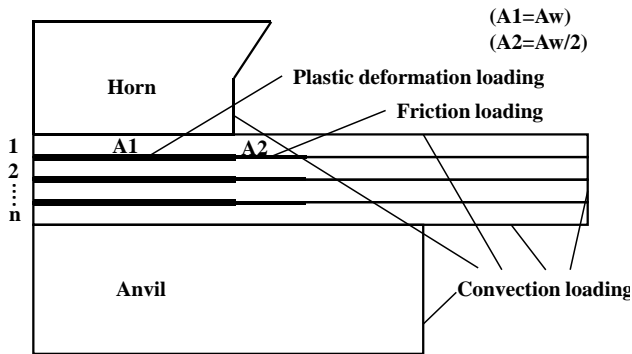
(3) Applying thermal force

Fig. 4. The thermal force in n layers of foils during ultrasonic welding.

When the multilayer foils are ultrasonically welded, the external thermal force of transient distribution consists of: plastic deformation loads, the friction loads and convection loads, wherein the plastic deformation heat flux density $Q_w^n(t)$ is applied to the plastic deformation zone A1. That is, the area below the horn-section area (A$_w$).

The frictional heat flux density $Q_{FR}^n(t)$ is applied to the friction zone area A2, which is half that of the horn section (A$_w$/2). The horn, amorphous alloy, anvil natural convection load with air is applied to the respective boundary as shown in Fig.4.

3. Results and discussion

3.1. The experiment results analysis of Fe$_{78}$Si$_9$B$_{13}$ amorphous alloy by ultrasonic welding
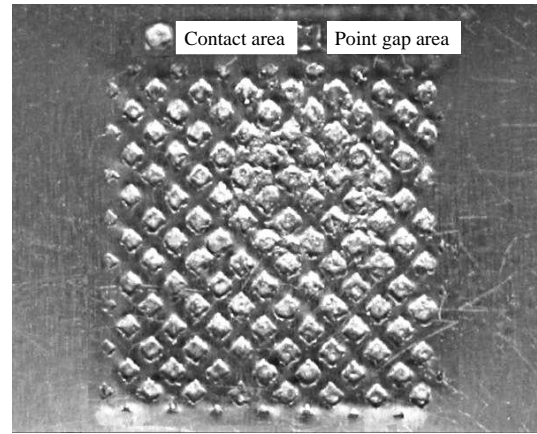

Fig. 5. Macroscopic surface structure of ultrasonically welded joints of multilayer Fe$_{78}$Si$_9$B$_{13}$ foils.

The horn and anvil surface of the welding metal spot have uneven texture. Under static pressure, the horn surface comes into contact with the specimen surface. Due to friction during ultrasonic vibration, welded area of the material appears to have an uneven texture. Therefore, the multilayer foil weld interface morphology as the contact area and point gap area. The macroscopic surface structure of the ultrasonically welded joints of multilayer Fe$_{78}$Si$_9$B$_{13}$ foils is shown in Fig. 5. As can be seen from the figure, the joints cross-section appears to have uneven thickness and shows a partial bend crack phenomenon.
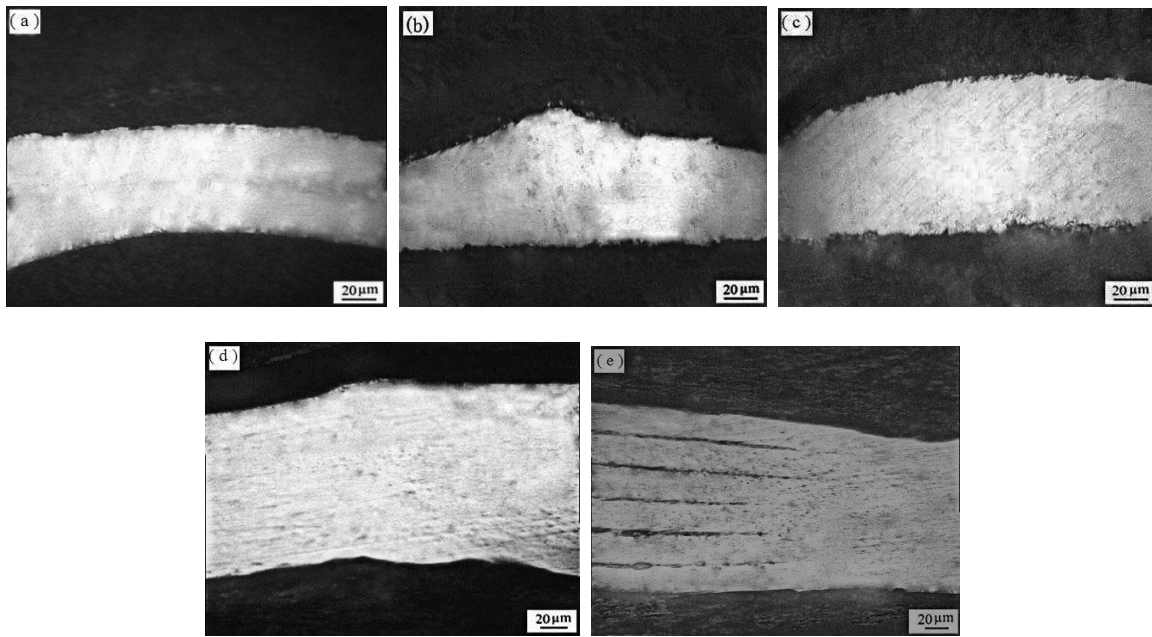
Fig. 6. Micrographs of weld joints of different layers of amorphous $Fe_{78}Si_9B_{13}$ alloys prepared by ultrasonic welding; (a) n=2 t=0.20 F=1.37×10³N; (b) n=3 t=0.22 F=1.37×10³N; (c) n=4 t=0.22s F=1.37×10³N; (d) n=5 t=0.22s F= 1.37×10³N;(e) n=6 t=0.22s F= 1.60×10³N.

Micrographs of different layers of welded $Fe_{78}Si_9B_{13}$ were observed to obtain the optimal welding parameters. As shown in Figs. 6(a), (b), (c), (d) and (e), n = 2–5. From fig. 6(a), (b), (c) and (d), it can be seen that the welded joints look good – no delamination, slag, pores, cracks or any other defects were observed.

These images indicate that the $Fe_{78}Si_9B_{13}$ foil welding interface is intact. Additionally, the microstructure did not change. To achieve the best weld joint by ultrasonic welding process, with the optimum surface and volume effects, a value of n = 6 was found to be ideal. From Fig. 6(e), it can be seen that at welding time of 220ms and the static pressure of 1.60×10³N, it was found to be difficult to make an effective weld joint due insufficient ultrasonic welding energy. Joint contact area formed a good joint, but the point gap area shows a large gap. The results show that the static pressure and atomic bonding play a decisive role in determining the weld joint quality.
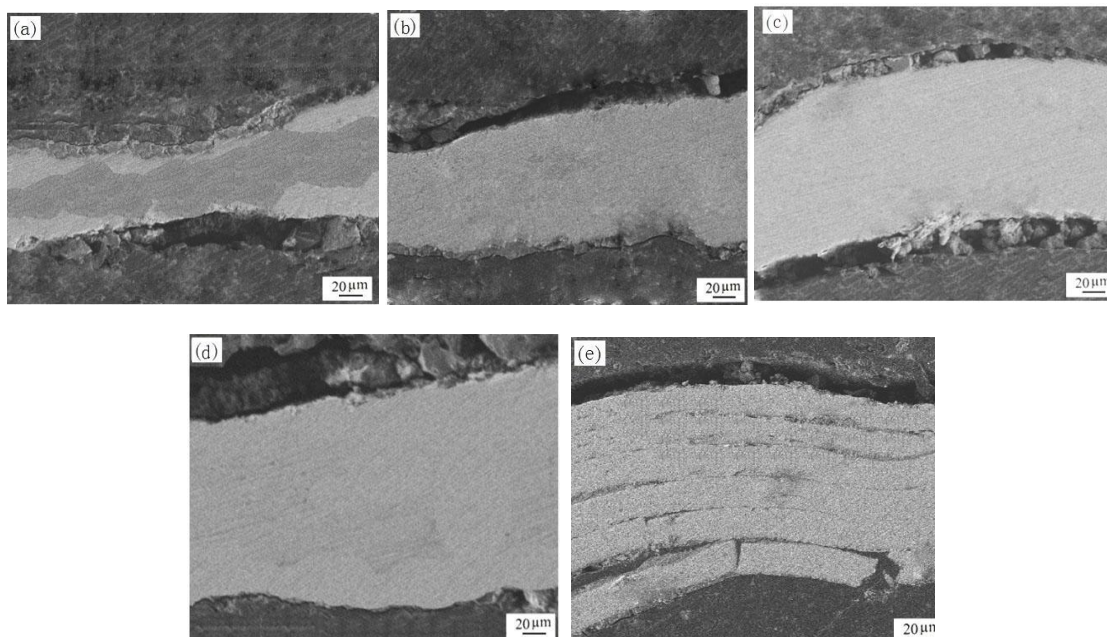

Fig.7. SEM image of $Fe_{78}Si_9B_{13}$ amorphous alloy foil welding joint (a) n = 2; (b) n = 3; (c) n = 4; (d) n = 5; (e) n = 6,

The ultrasonic welding time was 220ms, the welding pressure was 1.37×10³N and overlay of 2–6 layers was

used. Fig. 7 shows an SEM image of $Fe_{78}Si_9B_{13}$ amorphous alloy foil ultrasonic weld joint contact area. At n = 2, the contact zone of the joints appears welded, but some crystallization might have taken place near the weld zone. At n= 3–5, no grain boundaries, slag, pores, cracks or other defects were observed at the joint indicating a good weld joint. At n = 6, welded joint contact area shows large number of gaps and cracks, indicating that only a local weld joint was achieved effectively.
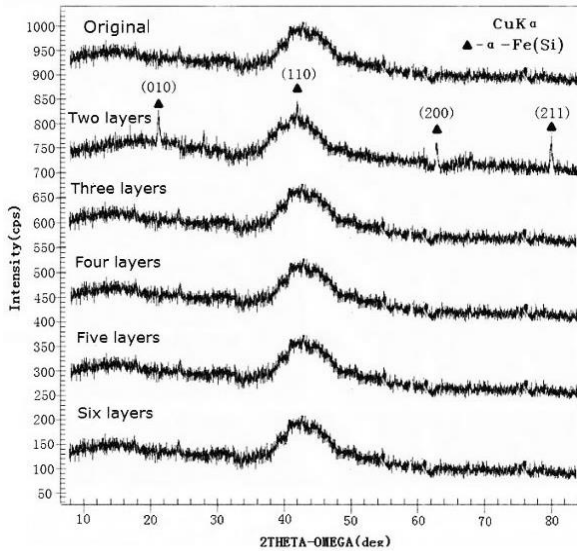

Fig. 8. The micro -X-ray diffraction pattern of amorphous Fe₇₈Si₉B₁₃ alloy welded joints interfacial contact area

Fig. 8 shows the micro -X-ray diffraction pattern of the amorphous $Fe_{78}Si_9B_{13}$ welded joints area (ultrasonic welding parameter t = 220ms, F =1.37×10³N). At n=2, the diffraction pattern of the post weld specimen shows sharp peaks near 21°, 42°, 63° and 80°. Analysis shows that these peaks refer to crystal planes (010), (110), (200) and (211) of the crystal phase α-Fe (Si). At $n = 3 – 6$, the diffraction pattern of the post weld specimen shows a scattered diffused peak indicative of an amorphous materials. No other sharp peaks were noticed. This shows that the material retained it amorphous structure even after welding.

Amorphous $Fe_{78}Si_{13}B_9$ is a multi-component amorphous system, which shows a high strain rate and super-plasticity in the super-cooled liquid phase [24-26]. In its solid state, it has a stress - strain rate sensitivity factor m' less than 0.2, its elongation ψ is less than 100%. However, when it is super-cooled, it shows strong superplastic characteristics, stress - strain rate sensitivity factor increases from 0.2 to 0.7, the elongation is more than 200%, and has a high thermal stability. If the temperature of the $Fe_{78}Si_{13}B_9$ amorphous material is maintained at the glass transition temperature, the material can maintain its amorphous structure for 10^3s [27]. It is because of the high thermal stability of the alloy

that it can avoid crystallization during the welding thermal cycle. The experimental results show that the ultrasonic welding time of 800ms (including the time of cooling to room temperature) is insufficient for multilayer foils is less than the iron base amorphous $Fe_{78}Si_{13}B_9$ by super cooled liquid - solid shift C curve tip time $(1–10^2$s) under the condition of continuous cooling [28]. So having multilayer foils help keep the material amorphous after ultrasonic welding.
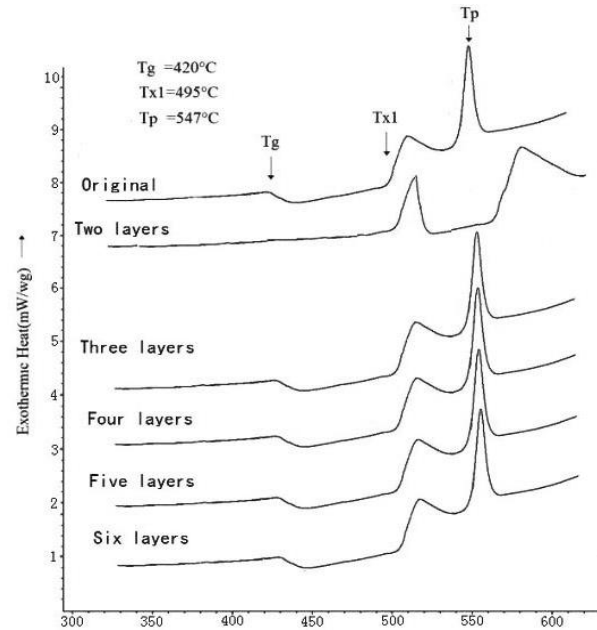

Fig. 9. DSC graph of the original amorphous and the multilayer Fe₇₈Si₁₃B₉ amorphous foil weld joint.

DSC graph of the original amorphous alloy as well as the post weld multilayer $Fe_{78}Si_{13}B_9$ amorphous foil is shown in fig. 9. The heating rate of 10 ° C / min. was used for the tests. The weld sample with the following conditions was used for the tests- ultrasonic welding parameter t=220ms, F=1.37×10³N. At n=2, the graphs indicate that the sample undergoes significant changes after ultrasonic welding which suggests that the material's atomic structure has changed in some way. The thermal properties of the joint are quite different from the initial amorphous material. At n=3–6, DSC curve of specimen shows graphs that are very similar to that of the original amorphous material. Specimen glass transition temperature T_g is 420 °C, the crystallization transition temperature T_{x1} is 495 °C and the crystallization peak temperature T_p is 547 °C; which is the same as that of the amorphous $Fe_{78}Si_{13}B_9$ alloy. Super cooled liquid region range is 75 °C. This indicates that the multilayer $Fe_{78}Si_{13}B_9$ foils does not undergo any structural changes, maintaining the original atomic structure after ultrasonic welding.
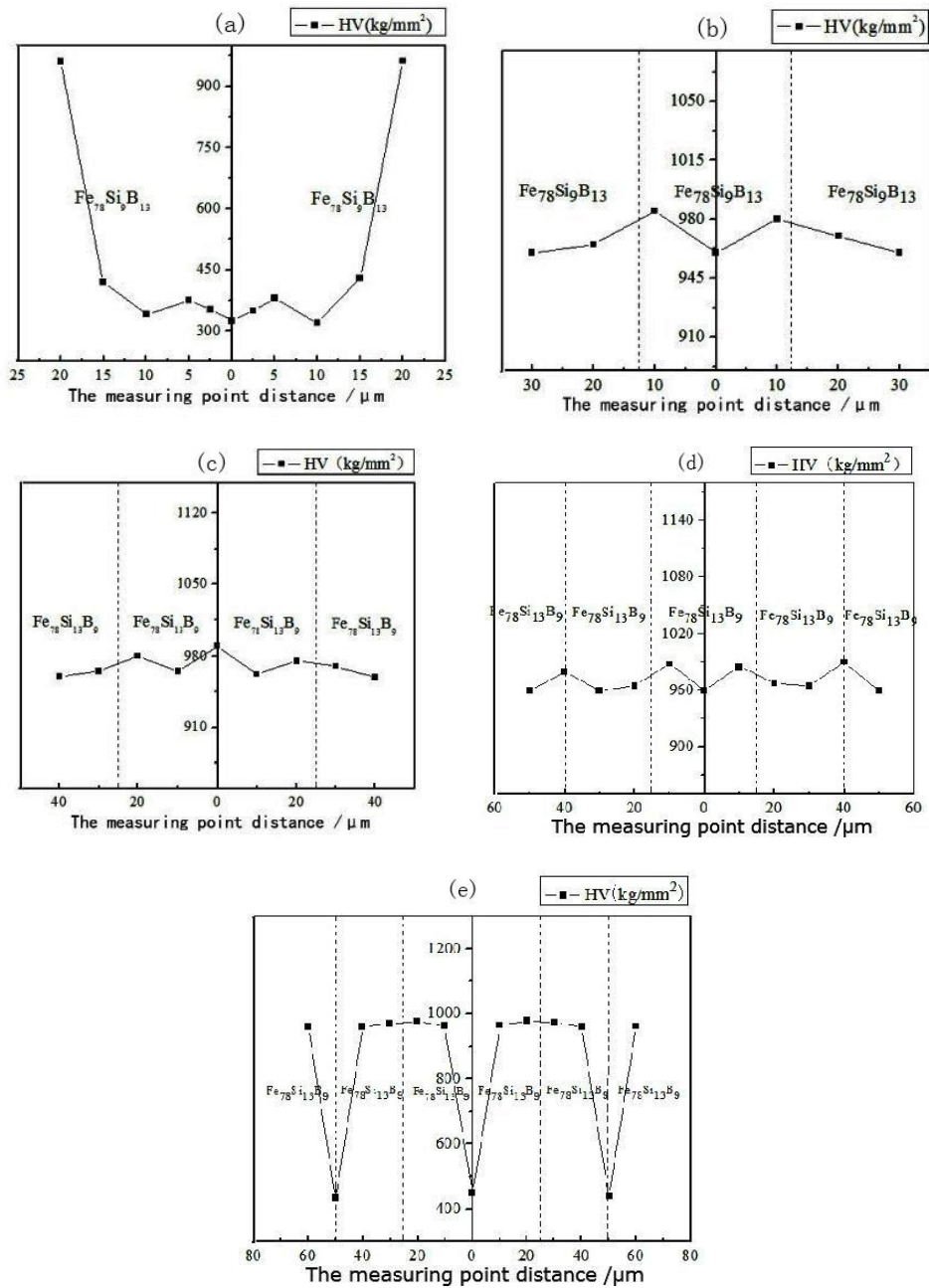
Fig. 10. Micro-hardness of weld joints of bulk amorphous alloy (a) n=2; (b) n=3; (c) n=4; (d) n=5; (e) n=6.

Fig. 10 shows the micro-hardness of the weld joint of the bulk amorphous alloy (ultrasonic welding parameter t=220ms, F=1.37×10³N). The micro-hardness of the starting amorphous alloy is 960HV. At n=2, the weld zone micro-hardness is 320 HV. The hardness of the specimen increases with increasing distance from the weld interface, and reaches a maximum of 970HV. As the amorphous material crystallizes, the hardness decreases, indicating that the structure of amorphous alloy in the weld zone has changed. At n=3–5, micro-hardness of the weld zone and heat affected zone increases slightly. A maximum hardness of 990 HV was achieved in the weld zone. Amorphous alloys show high deformation under static pressure and alternating shear

stress during the ultrasonic welding process. Simultaneously under the influence of volume effects and surface effects. When pressure is applied again, the deformation resistance increases, and consequently the hardness increases. There is a greater degree of deformation of the specimen in the weld zone, and therefore a higher hardness is observed. At n=6, the hardness of the weld joint at the weld zone is 440HV, and heat affected zone is slightly larger. This can be explained since the specimen shows a sharp drop due to a large gap between the contact weld surfaces, due to which the samples failed to form an effective weld joint. Hardness test show that the micro-hardness reduces quickly at the weld zone interface, while the heat affected

zone hardness is slightly increased due to the effect of deformation resistance.

Amorphous layers n	2	3	4	5	6
Edge maximum temperature T（℃）	259	234	223	216	187
Centre maximum temperature T（℃）	518	468	446	432	374

Table 3 shows the multilayer Fe$_{78}$Si$_{13}$B$_9$ amorphous alloy foil weld joints edge temperature distribution test results during the ultrasonic welding process (welding parameter t=220ms, F=1.37×10^{3}N). Theoretical study of ultrasound energy transfer suggests that the weld zone center temperature would be higher than the temperature of the joint edge. Transmission of ultrasonic energy to the central area of the edge of time is about 2 times, therefore the center maximum temperature of multilayer foil weld joint by ultrasonically welding can be approximately inferred. At n=2, the post weld specimen failed to avoid crystallization. At n=3–5, the maximum temperature at the center of the weld interface is lower than the amorphous Fe$_{78}$Si$_{13}$B$_9$ to crystal transition temperature. So after the ultrasonic welding, specimen forms a good weld joint. At n=6, the maximum

temperature at the center of the weld interface is 374℃ which is lower than the amorphous Fe$_{78}$Si$_{13}$B$_9$ alloy's glass transition temperature of 420℃. Therefore, the ultrasonic welding process fails to form a good weld joint in the specimen.

3.2. The finite element analysis of ultrasonic welding of Fe$_{78}$Si$_9$B$_{13}$ amorphous alloy

Fig. 11 shows the temperature field contours of Fe$_{78}$Si$_9$B$_{13}$ amorphous alloy welded ultrasonically (welding parameter- t=220ms; F=1.37×10^{3}N; n=2, 3, 4, 6). When the ultrasonic time or static pressure increases, the Fe$_{78}$Si$_9$B$_{13}$ foil interface temperature increases instantaneously. Since the maximum amount of plastic deformation in the foil happens between the first and second layers, the interface temperature here is the highest. At n=2, the maximum temperature at the weld interface is greater than the crystallization transition temperature of 495 ℃, hence the sample undergoes crystallization after welding. Weld interface temperature of the super-cooled liquid region is such that no crystallization takes place during welding, and an effective weld joint can be obtained. At n>=6, the weld interface maximum temperature is 420 ℃ which is less than the glass transition temperature, hence the foil deforms only elastically which makes forming an effective weld joint difficult.
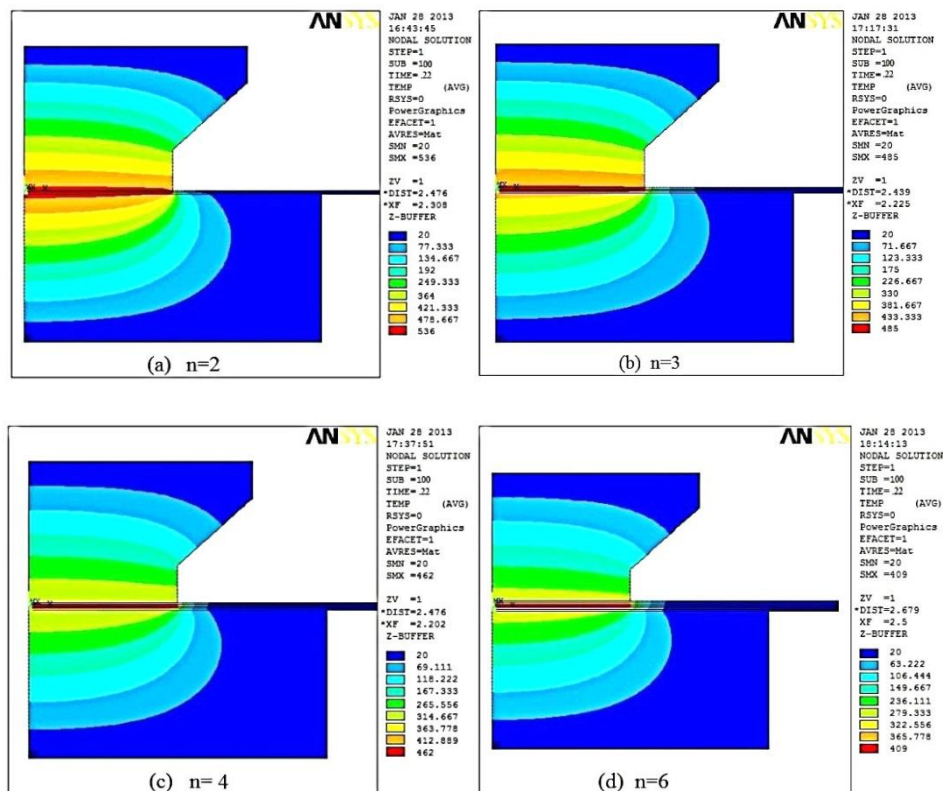

Fig. 11. The temperature field contours of multilayer Fe$_{78}$Si$_9$B$_{13}$ amorphous alloy foil during ultrasonic welding.
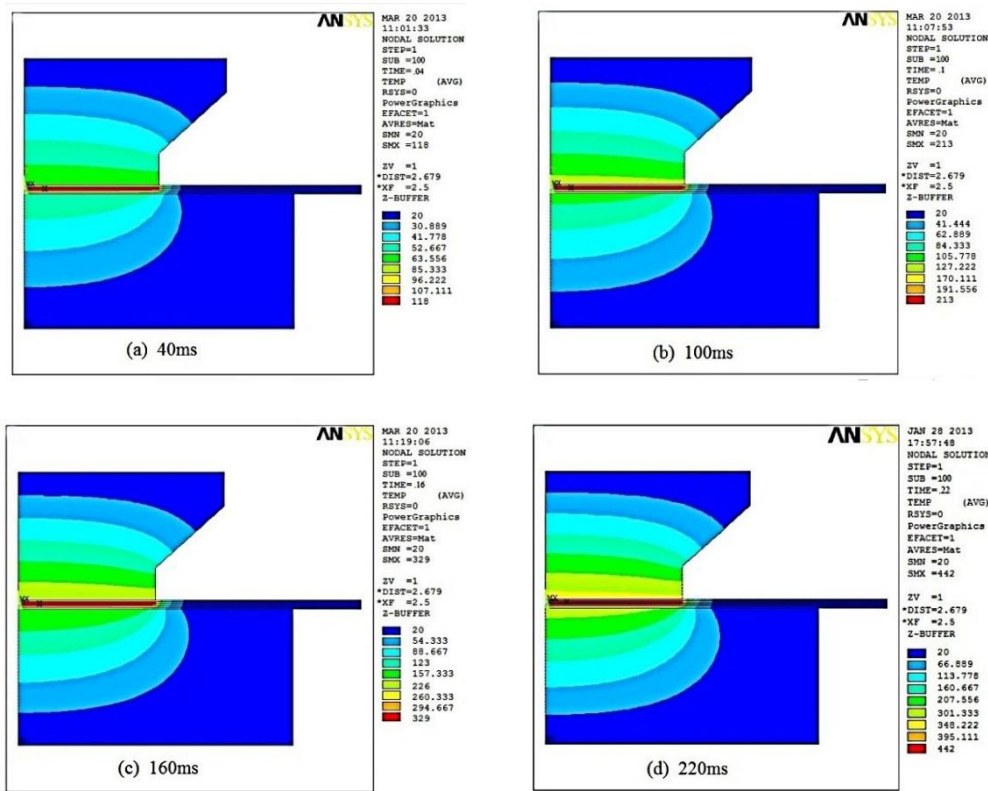
Fig. 12. The temperature field contours of 5 layers $Fe_{78}Si_9B_{13}$ amorphous alloy foil at different welding times during ultrasonic welding.

Fig. 12 shows the temperature field contours of 5 layers of $Fe_{78}Si_9B_{13}$ amorphous alloy foil during ultrasonic welding at a pressure of $1.37 \times 10^3 N$ and at different welding times. In the ultrasonic welding process, the interface temperature increases with increasing welding time. This is because as the welding time increases, the contact interfacial friction area increases. At an ultrasonic welding time of 40ms, the specimen contact surface temperature is low. When the ultrasonic welding time is 160ms, the specimen contact interface temperature rises, and reaches a maximum of 329 °C. However, at this temperature the material is only elastically deformed. When the ultrasonic welding time is 220ms, specimen contact interface temperature reaches a maximum of 442 ° C, which is less than the $Fe_{78}Si_9B_{13}$ crystal transition temperature. This is due to a high amount of plastic deformation at the interface region, and reduced heat transfer in to the surroundings causing retention of heat in the sample. Simulation calculation results indicate that 5-layer $Fe_{78}Si_9B_{13}$ amorphous alloy weld joints would maintain an amorphous structure up to an ultrasonic welding time of 220ms, which is consistent with the experimental results. The study suggests that the preparation of bulk amorphous alloys by ultrasonic welding is feasible.
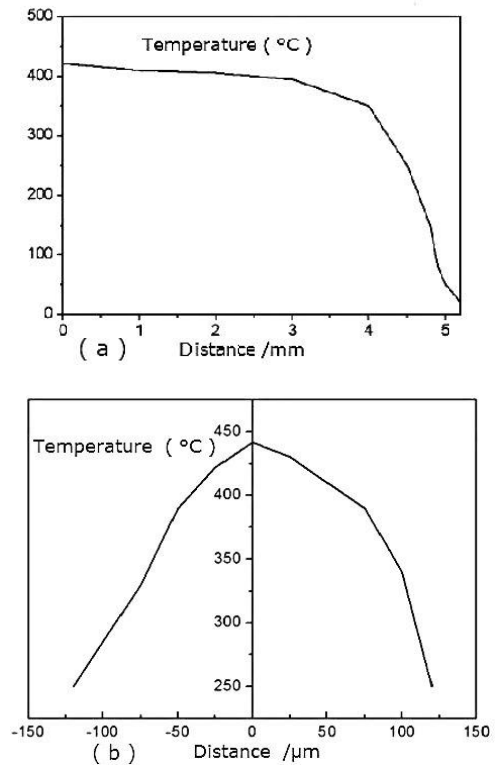

Fig. 13. The interface temperature curve of 5 layers of $Fe_{78}Si_9B_{13}$ amorphous alloy foil ultrasonic weld joint (a) X-axis (b) Y-axis.

Fig. 13 shows a graph with the interface temperature curves along the X-axis and Y-axis of the 5 layers $Fe_{78}Si_9B_{13}$ amorphous alloy foil welded for 220ms and under a static pressure of $1.37×10^3$N. On the X-axis, the temperature at 5mm from model symmetry center is close to room temperature. This suggests that during welding, the heat zone width is approximately 10mm in the X-axis direction, and the heat zone length is approximately 8mm on the Y-axis. Between consecutive layers, presence of gaps and thermal conductivity is a key factor affecting the size of the heat affected area.

4. Conclusions

In this paper, an ultrasonically welded multi-layer $Fe_{78}Si_9B_{13}$ foil was studied to determine its optimal welding parameters (n=5, A=35μm, f=20 kHz, F=1.37×10^3N, t=220ms). The samples were found to weld well and no crystallization of the amorphous material was observed. The process was used to successfully prepare bulk amorphous alloys.

Metallographic analysis was performed using scanning electron microscopy (SEM), micro-X-ray diffraction (XRD) analysis, differential scanning calorimetry (DSC) and Vickers micro-hardness testing method. Additionally, temperatures distributions of the samples during welding were measured. FEM analysis for the temperature distribution and resulting microstructure was also performed to confirm the experimental data.

This paper discusses preparation of a multi-layer amorphous $Fe_{78}Si_9B_{13}$ foil by ultrasonic welding method using axisymmetric thermal - structure coupled finite element model. Additionally, amorphous foil material model and heat source model were also evaluated. The ultrasonic welding multilayer amorphous foils temperature distribution was simulated under different welding parameters. This helped understand the effect of welding time on the welding temperature field distribution. The experimental results of bulk amorphous alloys made by ultrasonic welding are discussed.

Acknowledgements

References

[1] W. H. Wang, C. Dong, C. H. Shek, Mater Sci Techn R **44**(2-3), 45 (2004).

[2] A. Inoue, A. Takeuchi, Mater. Trans. **43**(8), 1892 (2002).

[3] W. K. Lement, R. Willens, P. Duwez, Nature **187,** 869 (1960).

[4] H. W. Kui, A. L. Greer, D. Turnbull, Appl. Phys. Lett. **45**(6), 615 (1984).

[5] A. Inoue, A. Shibata, T. Zhang, Mater Trans JIM **36,**1420 (1995).

[6] A. Inoue, T. Masumoto et al. Materials Science and Engineering A **173, 1** (1993).

[7] A. Inoue, T. Dchiai, Y. Hortio et al. Mater Sci. Eng. **649,** 179 (1994).

[8] T . D. Shen, R. B. Schwarz, Acta Mater. **49**, 837 (2000).

[9] X. H. Lin, W. L. Johnson, J. Appl. Phys, **78**, 6517 (1995).

[10] A. Peker, W. L. Johnson, Appl. Phys. Lett. **63**(17), 2342 (1993).

[11] Y. Kawamura, Y. Ohno, Scripta Materialia **45,** 127 (2001).

[12] B. Li, Z. Y. Li, J. G. Xiong, et al. Journal of Alloys and Compounds **413**, 118 (2006).

[13] Y. Yokoyama, N. Abe, K. Fukaura, et al. Materials Science and Engineering A **375–377**, 422 (2006).

[14] Y Kawamura, Materials Science and Engineering A **375–377**, 112 (2004).

[15] D. Wang, B. L. Xiao, Z. Y. Ma, et al. Scripta Materialia **60**(2), 112 (2009).

[16] H. S. Shin, J. S. Park, Y. C. Jung, et al. Journal of Alloys and Compounds **483,** 182 (2009).

[17] T. Shoji, Y. Kawamura, Y. Ohno, Materials Science and Engineering A **375–377,** 394 (2004).

[18] P. G. Debenedtti, F. H. Stillinger, Nature **410**, 259 (2001).

[19] C. H. Wong, C. H. Shek, Scripta Materialia **49,** 393 (2003).

[20] M. J. Greitmann, T. Adam, H. G. Holzweißig, et al. Tech. J. Weld. Allied Process **5**, 268 (2003).

[21] H. Kreye, M. Hammerschmidt, G. Reiners Scripta. Metallurgica **12**(11), 1059 (1978).

[22] M. Maeda, Y, Takahashi, M. Fukuhara et al. Materials Science and Engineering B **148,** 141 (2008).

[23] S. Elangovan, S. Semeer, K. Prakasan, et al. Journal of Materials Processing Technology **209,** 1143 (2009).

[24] M. Sasaki, Y. Kawamura, W. X. Gao, et al. Synthetic Metals **103**(1–3), 2662 (1999).

[25] A. P. Tsai, T. Kamiyama, Y. Kawamura, et al. Acta Materialia **45**(4), 1477 (1997).

[26] K. J. Takano, H. Harigae, Y. Kawamura, et al. Journal of Crystal Growth **171**(3–4), 554 (1997).

[27] Y. Kawamura, T. Shibata, A. Inoue, et al. Acta Materialia **46**(1), 253 (1998).

[28] Y. Kawamura, Y. Ohno, Scripta Materialia **45**(2), 127 (2001).

_____

[*]Corresponding author: zhuzhq01@163.com